Quantum Hall effect in InAsSb quantum wells at elevated temperatures

M. E. Bal,[1,2,*] E. Cheah,[3,4] Z. Lei,[3,4] R. Schott,[3,4] C. A. Lehner,[3] H. Engelkamp,[1,2] W. Wegscheider,[3,4] and U. Zeitler[1,2,†]

[1]*High Field Magnet Laboratory (HFML-EMFL), Radboud University, Toernooiveld 7, 6525 ED Nijmegen, The Netherlands*
[2]*Institute for Molecules and Materials, Radboud University, Heyendaalseweg 135, 6525 AJ Nijmegen, The Netherlands*
[3]*Solid State Physics Laboratory, ETH Zurich, CH-8093 Zurich, Switzerland*
[4]*Quantum Center, ETH Zürich, CH-8093 Zurich, Switzerland*

(Received 6 December 2023; revised 20 February 2024; accepted 29 April 2024; published 7 June 2024)

We have characterized the electronic properties of a high-mobility two-dimensional electron system in modulation doped InAsSb quantum wells and compare them to InSb quantum wells grown in a similar fashion. Using temperature-dependent Shubnikov-de Haas experiments as well as FIR transmission, we find an effective mass of $m^* \approx 0.022 m_e$, which is lower than in the investigated InSb quantum well, but due to a rather strong confinement still higher than in the corresponding bulk compound. The effective g-factor was determined to be $g^* \approx 24.1$. These results are also corroborated by $\boldsymbol{k} \cdot \boldsymbol{p}$ band structure calculations. When spin polarizing the electrons in a tilted magnetic field, the g-factor is significantly enhanced by electron-electron interactions, reaching a value as large as $g^* = 60$ at a spin polarization $P = 0.75$. Finally, we show that due to the low effective mass, the quantum Hall effect in our particular sample can be observed up to a temperature of 60 K.

DOI: 10.1103/PhysRevResearch.6.023259

I. INTRODUCTION

Since its discovery in 1980 by von Klitzing *et al.*, the quantum Hall effect (QHE) has been observed in a variety of high-mobility 2D systems, ranging from MOSFETs [1], quantum wells (QWs) [2,3], as well as intrinsic 2D materials [4–7]. This resulted in the definition of the resistance quantum, which enabled an incredibly precise determination of the fine-structure constant. Another breakthrough was achieved with the discovery of room temperature (RT) QHE in graphene, making it a convenient platform for performing metrological experiments [8–13]. Since the robustness of the QHE is, amongst others, governed by the Landau level (LL) spacing ($\Delta_{\mathrm{LL}} \sim 2000$ K at 30 T for graphene), InSb with its small effective mass ($m^*_{\mathrm{bulk}} = 0.014 m_e$), would conceptually also be a good material for the observation of a RT QHE. Optimally alloying InSb with InAs can reduce the effective mass even further, by utilizing the band bending commonly observed in ternary III-V compound semiconductors [14,15]. The QHE in InSb QWs has been investigated from several perspectives, e.g. FQHE [16,17], spin effects [16,17], high-current breakdown [3], and Ising quantum Hall ferromagnetism [18], whereas the literature on InAsSb QWs is less abundant. However, this material has become the subject of renewed interest because of its strong spin-orbit interaction [19,20] and small direct band gap [21].

In this paper, we present magneto-transport and far infrared (FIR) transmission data of InSb and InAsSb modulation doped QWs, enabling a direct comparison between the parent compound and the alloy. Firstly, the temperature dependence of Shubnikov-de Haas (SdH) oscillations enables the determination of the effective mass. Simultaneously, we acquire the temperature where the QHE disappears. The results for the effective mass are consistent with those obtained from cyclotron resonance (CR) measurements. Coincidence experiments in tilted magnetic fields are used to extract the g-factors, which are consistent with band-structure calculations based on $\boldsymbol{k} \cdot \boldsymbol{p}$ theory. Additionally, an interaction-induced enhancement of the g-factor for low filling factors, i.e., high spin polarization, is observed.

II. SAMPLES AND METHODS

Both the InSb as well as the InAsSb QW discussed in this manuscript, were grown by molecular beam epitaxy (MBE). The sample structure is based on the work of Lehner *et al.* [22], who systematically investigated the effect of employing buffer layers to overcome the lattice mismatch between (100) GaAs substrates and the InSb QWs [23]. On the other hand, the InAsSb QW was grown on a (001) GaSb substrate, thereby removing the AlSb/GaSb intermediate transition. The underlying $In_{1-y}Al_ySb/In_{1-x}Al_xSb$ ($x = 0.42$, $y = 0.54$) buffer was adjusted to the InAsSb QW lattice constant. The InSb ($InAs_{0.38}Sb_{0.62}$) 21 nm thick QW was surrounded by an $Al_{0.1}In_{0.9}Sb$ ($Al_{0.42}In_{0.58}Sb$) confinement barrier, which contained an asymmetric double-sided Si δ-doping layer, located 30 nm (44 nm) above and below the QW. The layer stack of both QW structures, as well as an

*Corresponding author: maurice.bal@ru.nl
†Corresponding author: uli.zeitler@ru.nl

investigation of the InAsSb QW and its As/Sb ratio via XRD, TEM, and EDX, are shown in Figs. 9 and 10 of the Appendix.

For the magnetotransport measurements both heterostructures were processed into a 880×25 μm^2 Hall bar using wet chemical etching. Ar-milling the top surface removes any contaminants and ensures that the successive layers of Ge/Ni/Au evaporated onto it, provide high quality Ohmic contacts. More information about the microfabrication can be found in Refs. [17,24]. The FIR transmission measurements were performed with an unprocessed piece of the same wafers, warranting a better signal-to-noise compared to the Hall bar. In order to suppress Fabry-Pérot interference effects in the transmitted light, the back of the sample was wedged under an angle of $\sim4^\circ$.

The transport measurements were performed in a ^{4}He bath cryostat, containing a variable temperature insert (VTI) with $T = 1.4$–300 K, which was placed inside a 38 T Florida-Bitter magnet. By mounting the sample on a rotating platform, it was possible to change the angle of the magnetic field *in situ*. Standard low-frequency lock-in techniques were used to acquire ρ_{xx} and ρ_{xy} of a 310×25 (405×25) μm^2 section of the InAsSb (InSb) Hall bar.

A Fourier transform infrared (FT-IR) spectrometer (Bruker VERTEX 80v) with a Globar broadband source, was used for the FIR transmission experiment. The IR radiation was coupled into a quasi-optical beamline, which guided the radiation towards a 33 T Florida-Bitter magnet. At the end of the beamline the radiation was focused into an oversized brass waveguide and passed through a polyethylene window, into a new-silver waveguide that was inside a ^{4}He bath cryostat. Before reaching the sample, the radiation was focused using a brass cone. The transmitted IR radiation was collected by a second brass cone, passed through another polyethylene window onto a Si bolometer that was kept at superfluid helium temperatures. The FT-IR spectra were measured at different fixed magnetic fields and normalized with a background spectrum, which was constructed from all spectra by taking the 90th percentile of each frequency, to obtain the transmittance $T(B) = T_m(B)/T_{\text{ref}}$.

III. RESULTS

In the following section, we will discuss the InAsSb QW in detail and compare these results to those obtained with the InSb QW.

A. SdH and quantum Hall measurements

As illustrated in Figs. 1(a) and 1(c), the magnetotransport measurements performed on an InAsSb QW Hall bar show clear SdH oscillations in ρ_{xx} and quantized plateaus in ρ_{xy} at $h/\nu e^2$, where ν is the filling factor. A carrier concentration of $n = 5.39\times10^{11}$ cm^{-2} and $n = 4.67\times10^{11}$ cm^{-2} was extracted from the classical Hall effect in small magnetic fields for the InAsSb and InSb QW, respectively. The corresponding mobility μ for both the InAsSb and InSb QW were 4.24×10^4 and 3.37×10^5 cm^2 V^{-1} s^{-1}. In an InAsSb QW at the lowest temperatures, we can resolve $\nu = 12$ in ρ_{xx}. This is considerably lower than for our high-mobility InSb QW where $\nu = 42$ was observed. The onset of quantum oscillations is governed by the condition $\mu_q B > 1$, where μ_q is the quantum mobility. Since the quantum mobility μ_q is one order of magnitude smaller than the transport mobility μ, which will be become apparent in the next section, we use the condition $\mu B \sim 10$ to estimate the onset of SdH oscillations. Based on this assumption we predict quantum oscillations to appear at $B \sim 2.4$ and ~0.3 T in the InAsSb and InSb QW, respectively. This is in good agreement with the experimental data presented in Figs. 1(a) and 1(c). In a similar fashion, spin splitting in the InAsSb QW starts to become visible at higher magnetic fields than in the InSb QW. This difference in mobility may be attributed to alloy disorder scattering, which is intrinsic for ternary compounds, or a possible alloy inhomogeneity in the QW [19]. In Figs. 1(b) and 1(d), we extract the quantum Hall activation energies of different filling factors, which will be discussed in greater detail in the upcoming section.

B. Effective mass, *g*-factor, and lifetime analysis

We start our investigation of the effective mass by introducing Ando's expression for the quantum oscillation amplitude in 2D systems [25]

$$\frac{\Delta\rho_{xx}(B,T)}{\rho_0(B)} \propto A_T(B,T)A_D(B)A_s, \tag{1}$$

where

$$A_T(B,T) = \frac{\frac{2C\pi^2k_BT}{\hbar\omega_c}}{\sinh\left(\frac{2\pi^2k_BT}{\hbar\omega_c}\right)}, \tag{2}$$

$$A_D(B) = \exp\left(\frac{-\pi}{\omega_c\tau_q}\right), \tag{3}$$

$$A_s = \cos\left[2\pi\left(\frac{g^*m^*}{2m_e} - \frac{1}{2}\right)\right], \tag{4}$$

Here $\omega_c = eB/m^*$ is the cyclotron frequency and C is a constant related to the oscillation amplitude at 0 K. In order to extract the effective mass from the temperature dependent suppression of the SdH oscillations, we first subtract a smooth magnetoresistance background ρ_0 from the ρ_{xx} data shown in Figs. 1(a) and 1(c), giving us the actual quantum oscillation amplitude $\Delta\rho_{xx}$ [see Figs. 2(a) and 2(c), respectively]. Figure 2(b) shows the suppression of some local maxima and minima of $\Delta\rho_{xx}$ with increasing temperature in an InAsSb QW, which was fitted with $A_T(B,T)$ to obtain an effective mass of $m^* \approx 0.022m_e$ [see inset Fig. 2(b)]. In comparison the effective mass of the InSb QW ($m^* \approx 0.028m_e$) was larger, confirming that alloying InSb with InAs indeed reduces the mass [see inset Fig. 2(d)]. It should be noted that both masses exceed what is reported in literature for a similar InSb heterostructure, where $m^* \approx 0.017m_e$ while the well width was comparable [17]. We attribute this to the fact that asymmetric doping can skew the potential well, effectively reducing its width and resulting in a higher mass due to stronger confinement. In the upcoming section we will give a more comprehensive analysis of the confinement enhancement based on band structure considerations.

Alternatively, one can also extract the effective mass from FIR transmission experiments, by tracking the CR as a function of magnetic field. As shown in Fig. 3(a), we observe clear

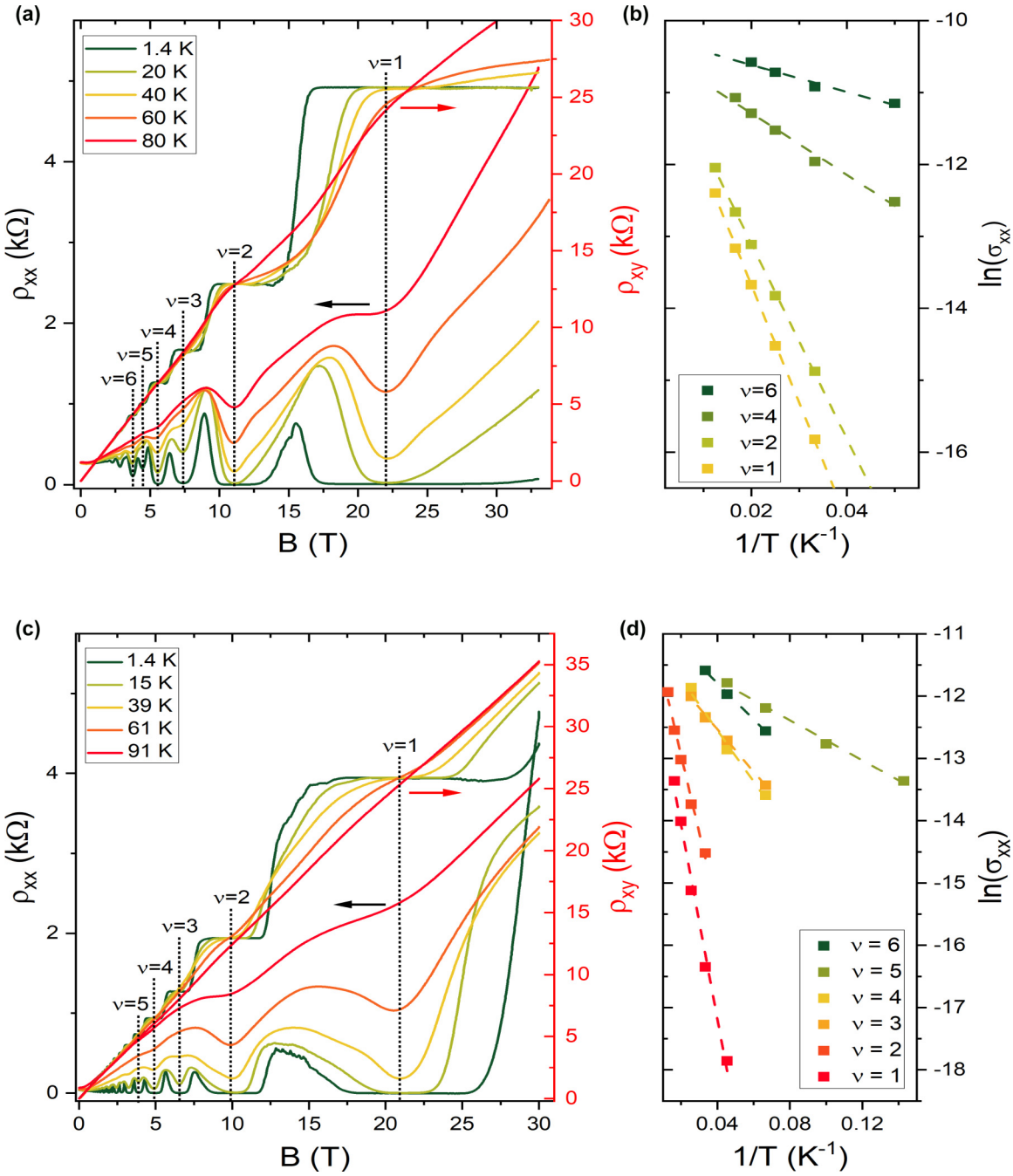

FIG. 1. Magnetic field dependence of ρ_{xx} and ρ_{xy} in an InAsSb (a) and InSb (c) QW at different temperatures. Temperature dependence of σ_{xx} minima in an InAsSb (b) and InSb (d) QW at multiple filling factors. Using the relation $\sigma_{xx} \propto \exp(-E_{act}/2k_BT)$, we extracted the activation energies from the linear fits.

dips in the transmittance, the signature of a CR, between one and four Tesla before the sample becomes opaque due to the InSb phonon absorption band. The position of the resonance was determined by fitting the spectra with a Lorentzian and was plotted against magnetic field in Fig. 3(b). By performing a linear fit of E_{CR} versus B, we can determine the effective mass, which was $m^* \approx 0.022m_e$. This result is in perfect agreement with the mass obtained from the temperature dependent SdH measurements.

It should also be noted that the CRs are quite broad, considering that the width goes from 2.4 to 4.3 meV due to the interaction with the phonon band. These line widths correspond to a scattering time of the order of 0.1 ps, which is comparable to the Drude scattering time determined below. For comparison, the width of the resonances in the InSb QW only increases from 1 to 1.7 meV within this field range [see Fig. 11(a) in the Appendix], corroborating our assumption that alloying introduces additional short range disorder

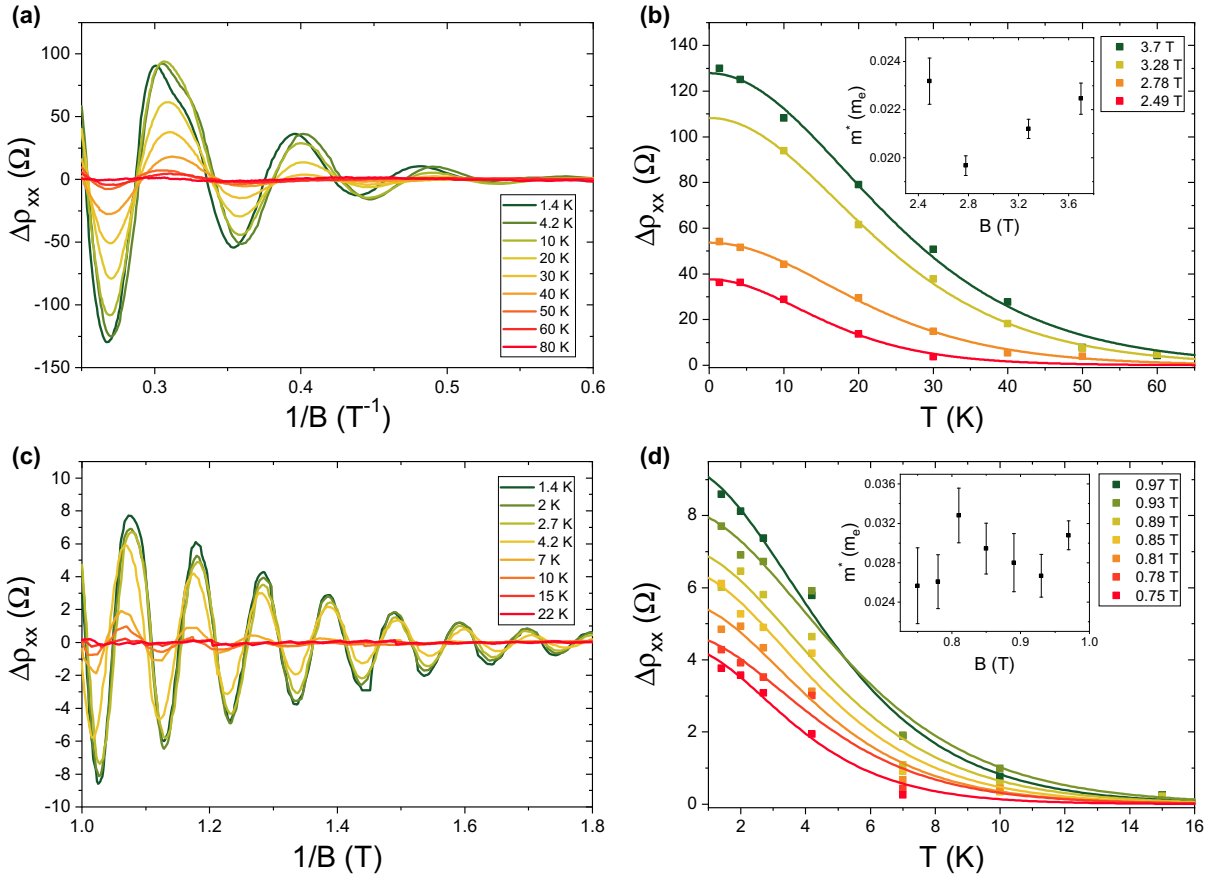

FIG. 2. Temperature dependence of the SdH oscillations in an InAsSb (a) and InSb (c) QW after subtraction of a magnetoresistance background. Only the field range where no spin splitting is observed is shown. Temperature dependence of quantum oscillation amplitudes at different magnetic fields in an InAsSb (b) and InSb (d) QW. The data was fitted with $A_T(B, T)$, which describes the thermal damping of quantum oscillations, to obtain the effective mass (see inset).

as the anion atoms will be randomly distributed over the available sublattice sites, which is in line with the lower mobility.

In Fig. 4, we extract the quantum lifetime τ_q from the slope of the linear fit of $1/B$ vs $\ln(\frac{\Delta\rho_{xx}}{\rho_0}A_T(B,T))$. Using the effective mass obtained above, τ_q was found to be 0.027 ps and was constant up to at least 20 K (see Fig. 4). The Drude scattering time $\tau_D = 0.53$ ps, which is determined with the classical Drude model, has the same order of magnitude as the scattering time extracted from the line width of the CRs. Knowing τ_D enables us to calculate the Dingle ratio as $\tau_D/\tau_q \approx 20$. The fact that this value is significantly larger than 1, means that long-range potential fluctuations are the dominant scattering mechanism [27].

As the temperature dependence of the longitudinal conductivity σ_{xx} at integer filling factors follows $\sigma_{xx} \propto \exp(-E_{\text{act}}/2k_BT)$, we can determine the activation energy $E_{\text{act},\nu}$ of the individual filling factors. From the linear fits presented in Fig. 1(b), we derive that $E_{\text{act},(1,2,4,6)}$ are 28.2, 23.4, 7.4 and 3.2 meV, respectively. By realizing that for odd filling factors $E_{\text{act,odd}} = g^*\mu_B B - \Gamma$ and neglecting the effect of the LL broadening Γ, we can calculate the effective g-factor. Therefore, at filling factor $\nu = 1$, we have $g^* \sim 21.9$. It has to be stressed that this value is an initial rough estimate, as we do not take into account the g-factor enhancement due to the exchange interaction. Plotting $E_{\text{act,even}}$ as a function of B and fitting this linear relation with the expression $E_{\text{act,even}} = \hbar\omega_c - g^*\mu_B B - \Gamma$, gives us an alternative method to determine the effective mass as well as a rough estimate of the LL broadening Γ [see Fig. 3(b)]. The activation energies underestimate the actual LL separation as they contain contributions from Zeeman splitting and LL broadening. Using the bare g-factor $g^* = 24.1$ acquired from coincidence measurements that are to be discussed later in the manuscript, we can correct for the Zeeman contribution. From these corrected activation energies we get an effective mass $m^* \approx 0.028m_e$, which is slightly larger than the one obtained from the temperature dependence of the SdH oscillations and FIR transmission. This discrepancy can be ascribed to the magnetic field dependence of the LL broadening Γ. Based on the offset of $E_{\text{act,even}}$ vs B, we can conclude that Γ has a lower bound of 7.4 meV. Using the relation $\Gamma = \hbar/\tau_q$ we can compare this lower bound for the LL broadening with the value extracted from the above mentioned quantum lifetime. The quantum lifetime corresponds to $\Gamma = 24.4$ meV, which is in reasonable agreement with the value derived from the activation energy if we keep in mind that the magnetic field dependence of the LL broadening is neglected.

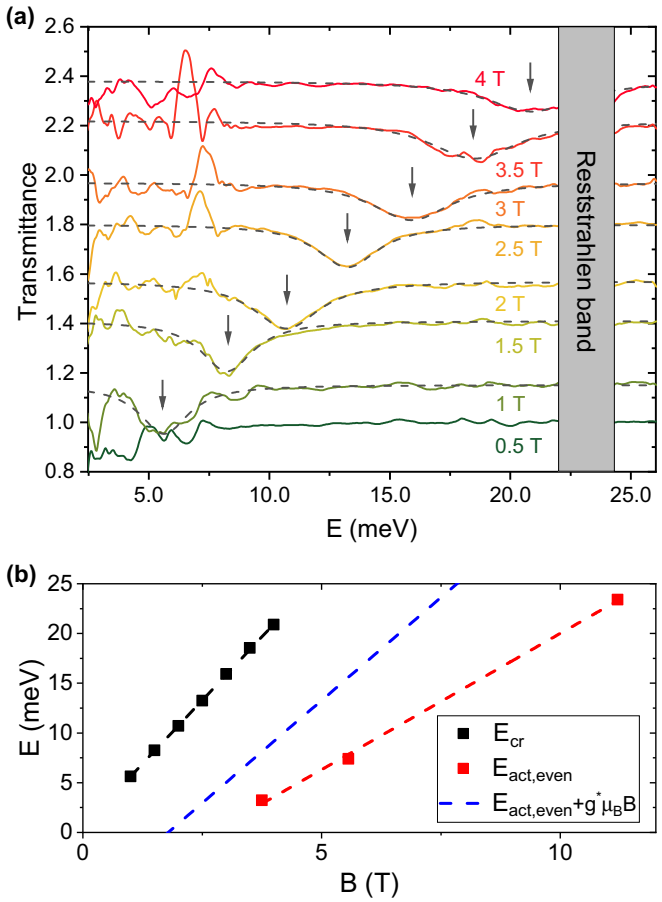

FIG. 3. (a) Transmittance as a function of energy for different magnetic fields in an InAsSb QW. The traces have a constant offset of 0.2. In the region between 3 and 6 meV the signal is fairly noisy due to lower signal strength and the pick up of electronic/mechanical noise. Due to the Reststrahlen band, the sample becomes completely opaque between 22 and 24 meV [26]. The arrows indicate the position of the CR determined from the Lorentzian fits (gray dashed line). (b) Cyclotron resonance and activation energy as a function of magnetic field. The corrected activation energies without the Zeeman contribution were also included (blue dashed line).

A similar analysis can be performed for the InSb QW, where the linear fits in Fig. 1(d) were used to extract $E_{\mathrm{act},(1,2,3,4,5,6)}$ and amounted to 26.7, 21.4, 5.9, 7.1, 2.8, and 5 meV, respectively. The magnetic field dependence of these activation energies, plotted in Fig. 11(b) of the Appendix, in combination with the linear relations for $E_{\mathrm{act,even}}$ and $E_{\mathrm{act,odd}}$ introduced above, can be used to obtain $g^* \sim 24.4$ and $m^* \approx 0.031 m_e$. The resulting effective mass is in reasonable agreement with the value procured with temperature dependent magnetotransport measurements, despite the fact that we neglect the g-factor enhancement due to the exchange interaction. Considering the difference between the effective masses derived from FIR transmission and the temperature dependence of the SdH oscillations, it is not possible to unambiguously identify a magnetic field dependent LL broadening in the corrected value for $E_{\mathrm{act,even}}$ like in the InAsSb QW. The lower bounds for the LL broadening Γ is 3.3 meV, which is smaller than the corresponding value for the InAsSb QW and

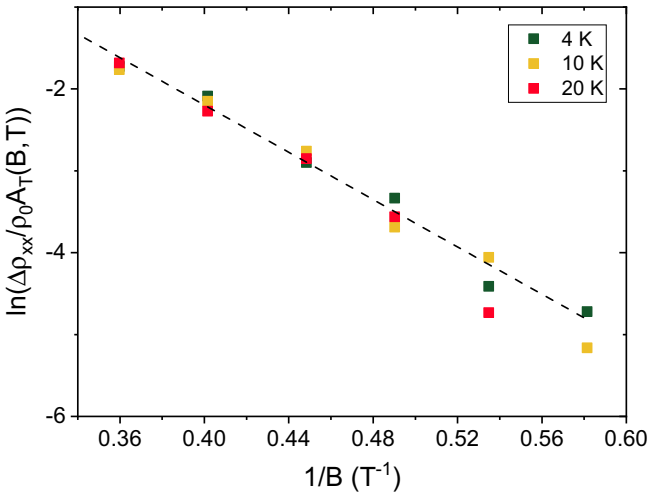

FIG. 4. Quantum lifetime determined from the linear fit of the exponential Dingle term in the Ando formula for the Shubnikov-de Haas effect in an InAsSb QW.

would be in line with the observation that the CRs are sharper in the InSb QW.

The activation energies derived above, can be compared with the temperature where the QHE disappears. In literature there are reports that the thermal energy at which the Hall resistivity is still quantized is roughly eight times larger than the energy gap between the levels [28]. Based on this phenomenological condition, we would expect the QHE in the InAsSb (InSb) QW to survive up to 41 or 34 K (39 or 31 K) for $\nu = 1$ and 2, respectively. Our magnetotransport measurements show that in both devices quantized quantum Hall plateaus survive up to 40 K [see Figs. 1(a) and 1(c)]. Consequently, we can conclude that the robustness of the QHE is in good agreement with the activation energies of the lower filling factors. On the other hand, in the InAsSb QW signatures of the QHE are present till 60 K, suggesting that the QHE is slightly more robust in this system as a result of the smaller mass.

C. Determination of confinement

Next, with calculations based on multiband $\boldsymbol{k}\cdot\boldsymbol{p}$ theory, we quantify confinement due to potential well skewing. First of all, we have to realize that the effective band gap E_g will be increased due to the confinement of the QW, which in the infinite potential approximation amounts to $E_{\mathrm{con}} = \pi^2\hbar^2/2L^2 m^*_{\mathrm{bulk}}$, where L is the QW width and m^*_{bulk} the effective mass of the bulk material. By only including the first order $\boldsymbol{k}\cdot\boldsymbol{p}$ terms, one uses a three-level model neglecting all other bands except the conduction and valence band, giving us an expression as in Ref. [27],

$$\frac{m_e}{m^*} = 1 + \frac{2m_e P^2}{\hbar^2(E_g + E_{\mathrm{con}})}. \tag{5}$$

If all $\boldsymbol{k}\cdot\boldsymbol{p}$ terms of the five closest bands at the Γ point including the spin orbit interaction are taken into account, one

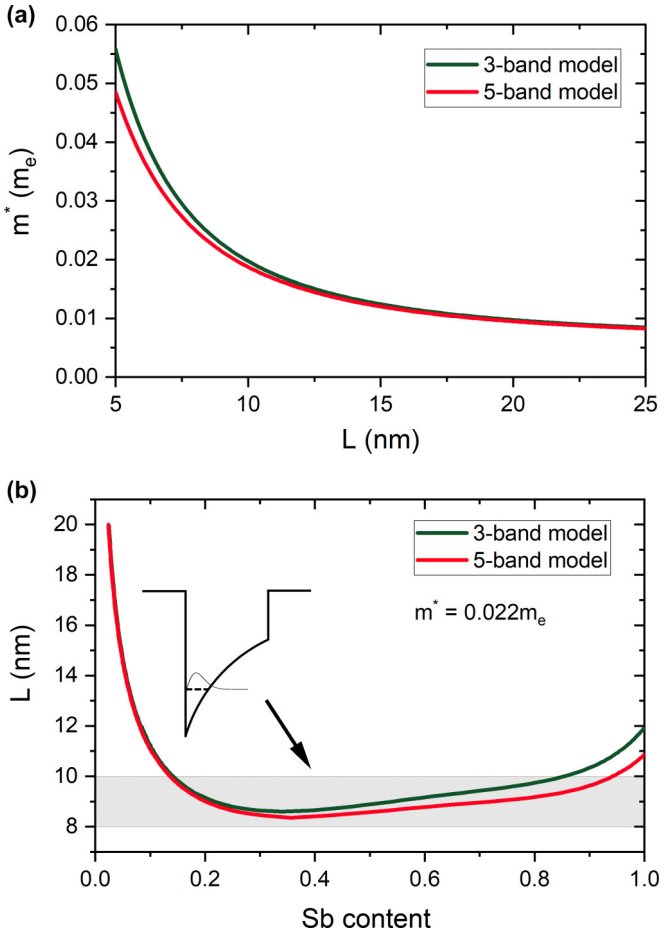

FIG. 5. With three and five band $\boldsymbol{k}\cdot\boldsymbol{p}$ theory, we calculate the dependence of the effective mass on the QW width (a) and the quantum well confinement as a function of the Sb content in $InAs_{1-x}Sb_x$ (b). In the latter, we use an effective mass of $0.022m_e$ and include a schematic depiction of the QW potential in the shaded area, illustrating the stronger confinement.

can express the effective mass as follows:

$$\frac{m_e}{m^*} = 1 + \frac{1}{3}\frac{2m_eP^2}{\hbar^2}\left(\frac{2}{E_g + E_{\text{con}}} + \frac{1}{E_g + \Delta_0 + E_{\text{con}}}\right) - \frac{1}{3}\frac{2m_eP'^2}{\hbar^2}\left(\frac{2}{E'_g - E_g + \Delta'_0} + \frac{1}{E'_g - E_g}\right), \tag{6}$$

where E_g, E'_g, Δ_0, Δ'_0, P and P' are band-edge parameters which can be found in literature [15,27]. All band-edge parameters have a quadratic dependence on the alloy composition, which deviates from the linear interpolation between two binary compounds by defining a so-called bowing parameter [15].

Figure 5(a) shows the effect of confinement on the effective mass for an optimally doped InAsSb QW, i.e., a Sb content of 62%. Here we assumed that the bowing parameter for E_g is similar to that of E'_g, P and P'. These calculations show that the effective mass becomes extremely sensitive to the QW width, as soon as the well becomes thinner than 15 nm. Similarly, we can determine the dependence of the QW width on Sb content x when $m^* = 0.022m_e$ for both the three- and five-band model

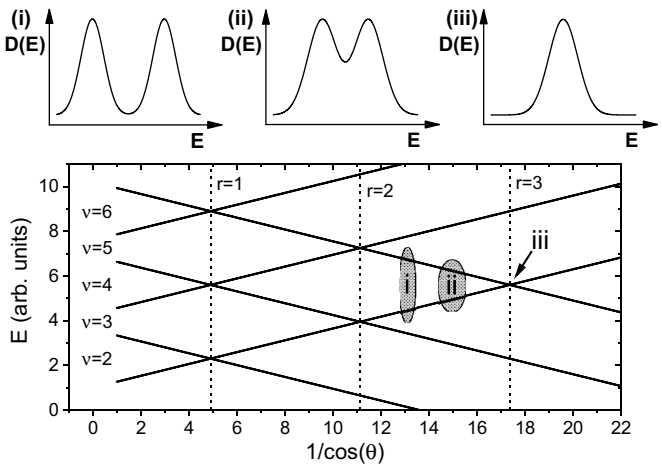

FIG. 6. Schematic representation of the principle behind a coincidence measurement, where one can see the opening and closing of the energy gap between even and odd Landau states. The position of the coincidences for even and odd filling factors is indicated by the dotted lines. In the three top panels we have plotted cross sections of the density of states at different angles, which correspond to the highlighted region between the Landau levels.

[see Fig. 5(b)]. In both cases, we see an abrupt increase in confinement as x is increased from 0 to 0.1, after which the dispersion starts to flatten off and eventually decreases again. EDX scans of the QW, shown in Fig. 10, confirm the presence of both As and Sb, which in conjunction with the fairly flat dispersion around the desired Sb content of 0.62, suggest that the QW width will most likely lie between 8 and 10 nm. This rather strong confinement could thus explain the relatively high effective masses we have reported earlier on.

D. Coincidence measurement

In this section we will discuss the interaction-induced enhancement of the g-factor as a function of spin polarization. Due to this enhancement, the g-factor can become much larger than predicted by $\boldsymbol{k}\cdot\boldsymbol{p}$ theory in the single-particle picture [16]. To investigate this effect, we have performed coincidence measurements. The principle of a coincidence measurement, is to change the ratio between the LL spacing and the Zeeman energy by varying the angle θ between the direction of sample normal and total applied magnetic field B_{tot} [see inset Fig. 7(a)]. Here we utilize the fact that the LL energy $\hbar\omega_c = \frac{\hbar eB_\perp}{m^*}$ is proportional to the perpendicular field component $B_\perp$, whereas the Zeeman energy depends on B_{tot}. Let us define the parameter r, which is the ratio between these two energies, i.e., $r = g^*\mu_B B_{\text{tot}}/\hbar\omega_c$. Since $B_\perp = cos(\theta)B_{\text{tot}}$ and using the definition of the Bohr magneton ($\mu_B = e\hbar/2m_e$), we can rewrite this expression as $rcos(\theta) = g^*m^*/2m_e$. For the case $r = 1$, the Zeeman splitting $g^*\mu_B B_{\text{tot}}$ equals the LL spacing $\hbar\omega_c$, meaning that for even filling factors the Landau states with opposite spins have the same energy, closing the energy gap between them. A similar reasoning holds for $r = 2$, but now the spin splitting is twice as large as the LL spacing, resulting in the suppression of the odd filling factors. Thus, the longitudinal resistivity minima appear only at odd or even

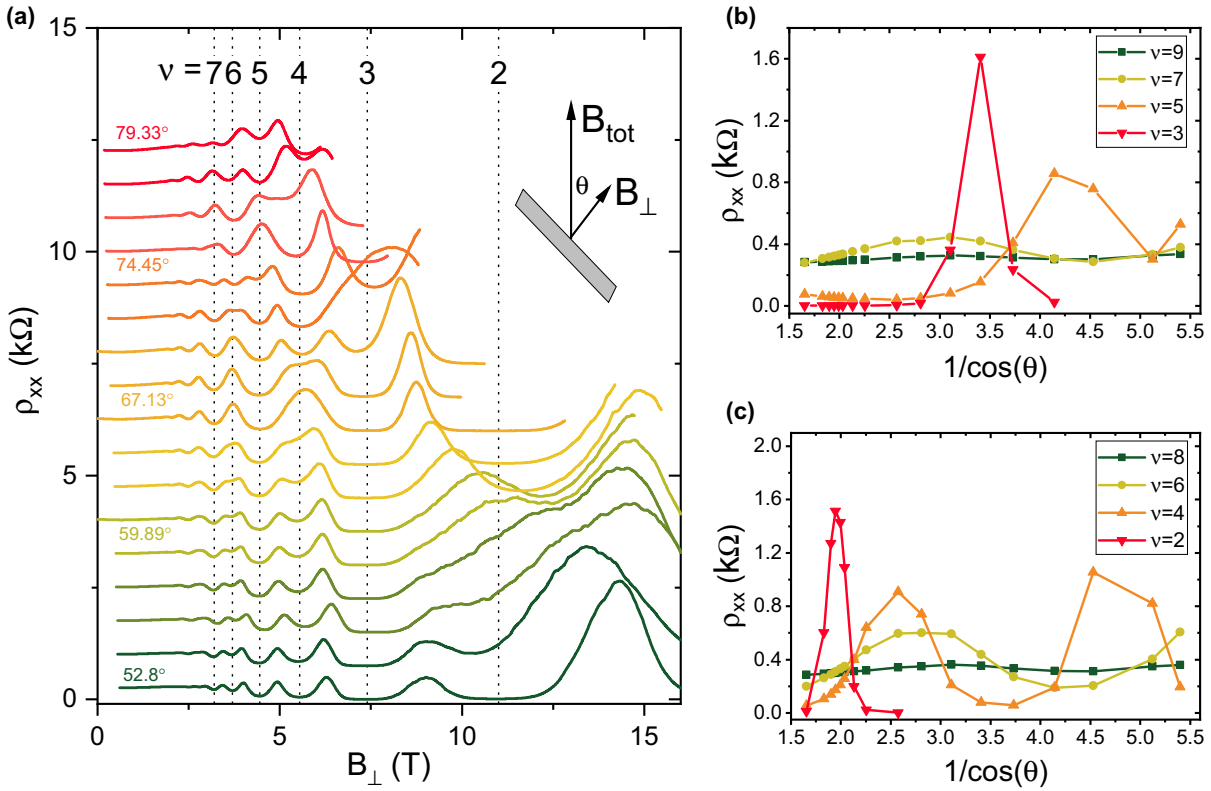

FIG. 7. (a) Angle dependence of ρ_{xx} in an InAsSb QW, where the angle was determined by aligning the $\nu = 5$ minima. The curves have a constant offset of 750 Ω. [(b) and (c)] Show ρ_{xx} as a function of θ for odd and even filling factors, respectively.

filling factors for $r = 1$ and $r = 2$, respectively. The opening and closing of the energy gaps is schematically depicted in Fig. 6. In this schematic representation, we have not taken into account the effect of g-factor enhancement, which means that the respective coincidences for odd and even filling factors occur at the same angle.

Figure 7(a) shows the result of our coincidence measurement, where we measured ρ_{xx} as a function of $B_\perp$ at angles ranging from $\theta = 53^\circ$ to 79°. The slope of the Hall signal was used to provide a rough estimate of the angle θ, which was subsequently optimized by aligning the $\nu = 5$ or $\nu = 6$ minima. Such optimization is required as a small error in the angle can significantly misalign the minima, hindering the accurate determination of the coincidence. However, it should be noted that the angles obtained from the Hall resistivity and SdH minima agree within better than 1% with each other. At each filling factor, indicated by the dashed lines, we monitor the evolution of ρ_{xx} as the angle is increased. The cross-sections of these traces are plotted in Figs. 7(b) and 7(c) for odd and even filling factors, respectively. It becomes apparent from the position of the maxima that the g-factor is not universal for the individual filling factors, as the coincidences occur at different angles. With the expression for r we can relate these coincidences to g^*m^*, which is proportional to the spin susceptibility $\chi = g^*m^*/2\pi\hbar$ in 2D systems [29], or equivalently to g^* after normalizing it with m^*. Figure 8 shows the dependence of g^*m^* on the spin polarization P, defined as $P = r/\nu$. The data displays a monotonic increase with spin polarization and g^* can become as large as 70 when the system is fully spin polarized at $P = 1$. Such an enhancement of the g-factor with a linear increase as a function of polarization was also reported recently in an undoped InSb QW [16] and has indeed been observed longer ago in GaAs-based 2DESs [30,31] and graphene [32]. It can be explained by the effect of electron-electron interaction leading to an exchange enhanced spin splitting within a Landau level [33,34] which

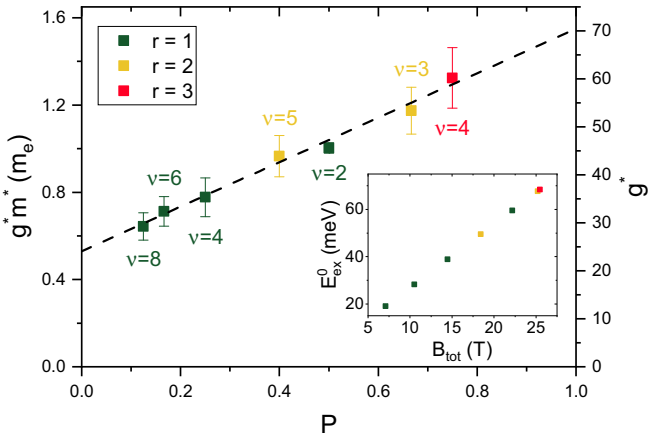

FIG. 8. g^*m^* as a function of P. Using the effective mass obtained by from the mass analysis, $m^* = 0.022m_e$, one can determine the effective g-factor. The corresponding g^* values are shown on the right-hand side axis. The inset displays E_{ex}^0 as a function of B_{tot}. The exchange parameter was extracted from the linear fit of g^*.

allows us to express the effective g-factor as

$$g^* = g_0^* + \frac{E_{\rm ex}^0 P}{\mu_B B_{\rm tot}}, \tag{7}$$

where g_0^* is the bare g-factor of the band electrons and $E_{\rm ex}^0$ is the exchange parameter [30,31]. From the experimentally observed linear dependence of g^* on the polarization we can then extract $E_{\rm ex}^0$ as a function of the total magnetic field as plotted in the inset of Fig. 8. The exchange parameter $E_{\rm ex}^0$ increases linearly with magnetic field since the separation of the neighboring Landau levels of opposite spin becomes more pronounced with respect to LL broadening. It is significantly larger in InAsSb (28 meV at 10.5 T) than in, for example, graphene (11.2 meV at 10 T [32]), a 2DES with a comparable large Ladau level separation which points towards stronger electron-electron interactions in our system. At the same time, as mentioned earlier, we now see that the value for the g-factor obtained from the activation energies when the field was perpendicular to the sample, should be treated as the bare g-factor of an unpolarized 2DES, i.e., $g^* = 24$ at $P = 0$.

Next, we will compare this result to $\boldsymbol{k}\cdot\boldsymbol{p}$ theory, where g^* is given by

$$g_0^* = 2 - \frac{2}{3}\frac{2m_e P^2}{\hbar^2}\left(\frac{1}{E_g + E_{\rm con}} + \frac{1}{E_g + \Delta_0 + E_{\rm con}}\right) + \frac{2}{3}\frac{2m_e P'^2}{\hbar^2}\left(\frac{1}{E_g' - E_g} + \frac{1}{E_g' - E_g + \Delta_0'}\right), \tag{8}$$

such as in Ref. [27]. From this expression, we get $g^* = 39.9$ if we take $L = 8$ nm and $x = 0.62$. Like in the previous section, the band-edge parameters were determined using a quadratic interpolation between the two binary compounds. The obtained g-factor is larger than the experimentally determined value. This could be explained by the uncertainty in the two independent parameters, as g^* strongly depends on the values used for the calculation.

IV. CONCLUSIONS

In summary, we have shown that by alloying InSb with InAs, we can reduce the effective mass. The masses extracted from the CRs are in good agreement with those obtained from the temperature dependent SdH measurements. The fact that the masses are larger than the bulk values can be ascribed to a strong 2D confinement. The QHE is observed up to 60 K, which is in line with the obtained activation energies. Also, an interaction-induced enhancement of the g-factor was observed with the coincidence method. At the largest spin polarization, g^* can be as large as 60. From the linear fit of the g-factor as a function of spin polarization we can extract values for the exchange parameter, which are significantly larger than those reported for graphene at comparable magnetic fields. To conclude, we have presented important proof-of-principle experiments on InAsSb QWs, a promising system with the potential of realising a low mass, high g-factor system.

ACKNOWLEDGMENTS

This work was supported by HFML-RU/NWO-I, member of the European Magnetic Field Laboratory (EMFL). It is part of the research programme "HFML-FELIX: a unique research infrastructure in the Netherlands. Matter under extreme conditions of intense infrared radiation and high magnetic fields" with Project No. 184.034.022 financed by the Dutch Research Council (NWO). We also acknowledge financial support from the Swiss National Science Foundation (SNSF) and the National Center of Competence in Science "QSIT-Quantum Science and Technology."

APPENDIX

1. Sample characterization

The layer stack of InSb, along with the InAsSb quantum wells (QWs), is illustrated in Fig. 9. Further insights into the characteristics of the InSb QW can be found in the works of Christian Lehner [22,23]. Utilizing these investigations, adjustments were made to the buffer structure of the InAsSb QW sample in order to achieve a nearly lattice-matched InAlSb barrier enveloping the QW. For the intended $InAs_{0.38}Sb_{0.62}$ QW, this adaptation resulted in an $In_{0.46}Al_{0.54}Sb/In_{0.58}Al_{0.42}Sb$ buffer structure.

The fabrication of the samples took place using a molecular beam epitaxy (MBE) Veeco Gen II system, with As and Sb being supplied via valved cracker sources. The temperatures of the As and Sb crackers were set at 750 °C and 700 °C, respectively. A pyrometer was employed to measure the substrate temperature. The growth rates of group III elements were determined through the analysis of Reflection High-Energy Electron Diffraction (RHEED) oscillations. The V/III ratios were then deduced from these growth rates of group V and group III elements.

The growth rate of As (Sb) was derived by tracking As (or Sb) oscillations using the following method. Initially, the As

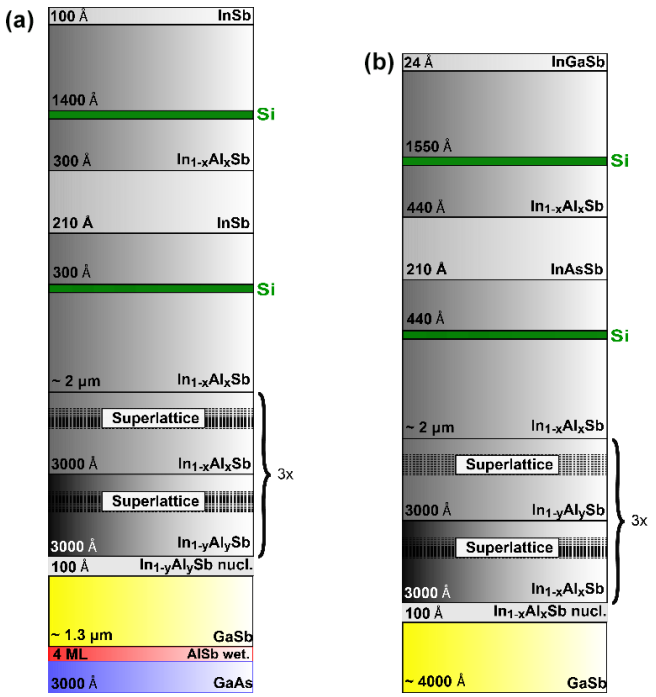

FIG. 9. Layer stack of the InSb QW structure (a) (with $x = 0.1$, $y = 0.3$) and the InAsSb QW structure (b) (with $x = 0.42$, $y = 0.54$).

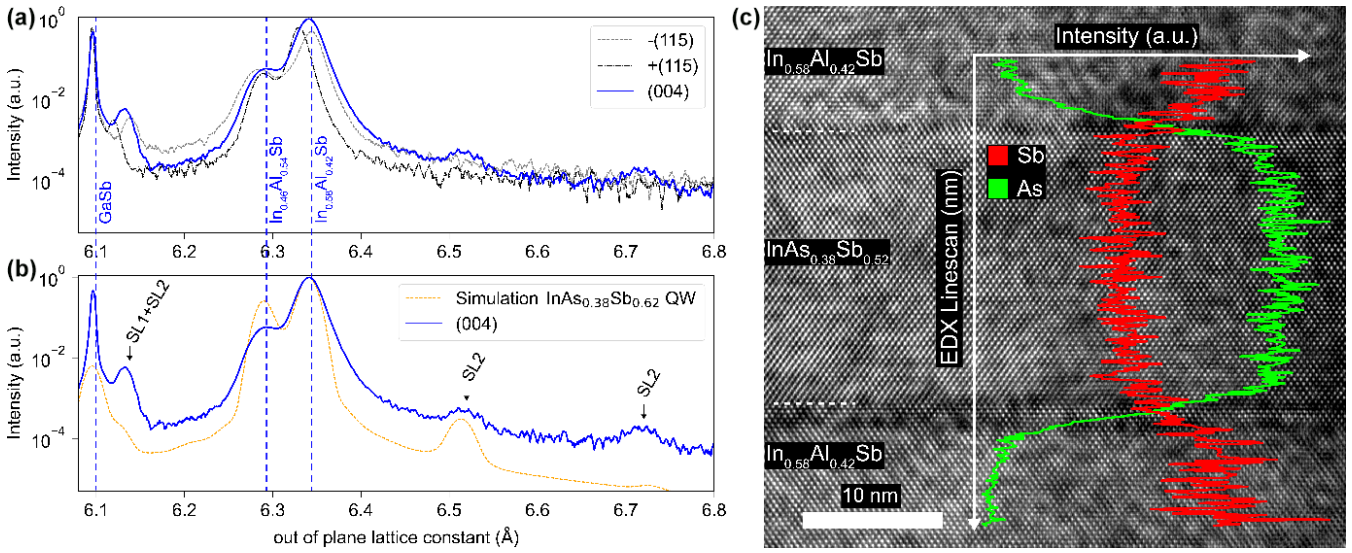

FIG. 10. (a) The x-ray diffraction measurements depict symmetric (004), asymmetric (115-), and (115+) scans. These x-ray rocking curves reveal the diffraction peaks of the GaSb substrate, including the AlSb/GaSb superlattice (SL1), the $In_{46}Al_{54}Sb/In_{58}Al_{42}Sb$ buffer, and satellite peaks of the $In_{46}Al_{54}Sb/In_{58}Al_{42}Sb$ superlattice (SL2). The peak corresponding to the InAsSb quantum well (QW) either coincides as expected with the $In_{58}Al_{42}Sb$ Layer peak or is relatively weak. The asymmetric rocking curves reveal that the $In_{58}Al_{42}Sb$ layer is slightly strained (with 95% relaxation). (b) A simulation of the symmetric (004) x-ray rocking curve of the $InAs_{0.38}Sb_{0.62}$ QW heterostructure is presented. (c) A transmission electron microscopy (TEM) image demonstrates the InAsSb QW surrounded by InAlSb wells. Qualitative evidence of As atoms in the QW layer is substantiated by the energy-dispersive x-ray (EDX) linescan.

(Sb) flux was terminated, and approximately 10 monolayers (MLs) of Ga were deposited onto the surface of GaAs (GaSb) at a rate of 0.5 Å/s and a temperature of 570 °C (480 °C). Immediately thereafter, As (Sb) was introduced at a selected valve setting, resulting in distinct and well-defined RHEED oscillations. For the InAsSb QW, an As (Sb) flux corresponding to a GaAs (GaSb) growth rate of 0.7 Å/s (4.8 Å/s) was employed. The $In_{0.46}Al_{0.54}Sb/In_{0.58}Al_{0.42}Sb$ buffer and the InAsSb QW were grown with a constant InAs (InSb) growth rate of 1.4 Å/s (1.7 Å/s) at a substrate temperature of 430 °C.

The composition of $InAs_xSb_{1-x}$ layers is influenced not only by the appropriate As/Sb flux ratio but also by other growth conditions, including the growth temperature and the specific As and Sb species from the valved cracker sources [22]. To ensure accurate composition control, thicker $InAs_xSb_{1-x}$ layers on an $In_{1-y}Al_ySb/In_{1-x}Al_xSb$ buffer were utilized as a reference, and their composition was calibrated using (004) x-ray diffraction measurements.

Figure 10(a) displays x-ray rocking curves of the final InAsSb QW heterostructure in the symmetric (004) direction along with the complementary directions (115-) and (115+). The anticipated peak of the $InAs_{0.38}Sb_{0.62}$ QW either coincides with the peak of the $In_{0.58}Al_{0.42}Sb$ layer or exhibits a weak signal due to the relatively thin nature of the QW in comparison to the buffer structure. A simulation of the x-ray rocking curve for this heterostructure [Fig. 10(b)] confirms the validity of this assumption. Considering the limitations imposed by the resolution of the x-ray equipment and fluctuations in the flux measurement, we estimate the As content to fall within a range of 33% to 38%. The faint satellite maxima emerge due to $In_{0.46}Al_{0.54}Sb/In_{0.58}Al_{0.42}Sb$ superlattices in the buffer (SL2) and an AlSb/GaSb superlattice in the GaSb layer (SL1). The $InAs_{0.38}Sb_{0.62}$ QW is examined via TEM and EDX. The EDX linescan qualitatively confirms the presence of As atoms in the QW layer.

A qualitative assessment of the strain in the QW and the buffer can be inferred from measurements using the asymmetric diffraction geometry. The noncoincident maxima positions of $In_{0.58}Al_{0.42}Sb$ indicate a slightly strained pseudomorphically grown QW (∼95% relaxation). Conversely, the maxima of $In_{0.46}Al_{0.54}Sb$ overlap, indicating relaxation in these layers.

2. FIR transmission InSb QW

The transmittance spectra contain CR features all the way up to 30 T [see Fig. 11(a)]. In the field range between 11 and 18 T, there are two distinct CR dips present due to the nonequidistant LL spacing stemming from the nonparabolicity of the bands. This nonparabolicity can be clearly seen in the nonlinear magnetic field dependence of the CR energy [see Fig. 11(b)]. Using $\boldsymbol{k}\cdot\boldsymbol{p}$ perturbation theory, we can self-consistently calculate the LL fan diagram and identify the LL transitions governing the resonances. These calculations show that the upper and lower branch of resonances are related to transition between the first and second Landau level with spin-up and spin-down electrons, respectively. This would explain the disappearance of the lower CR branch around 20 T, as the corresponding LL is almost completely depopulated close to $\nu = 1$ [see Fig. 1(c)]. The effective mass can be determined from the low-field data in Fig. 11(b), where the dispersion is still linear, giving us $m^* \approx 0.025m_e$. This value is noticeably smaller than the value extracted from the transport data. Such a discrepancy could originate from the fact that the FIR transmission measurements were performed with a different piece of the wafer, which can have different values for the effective mass.

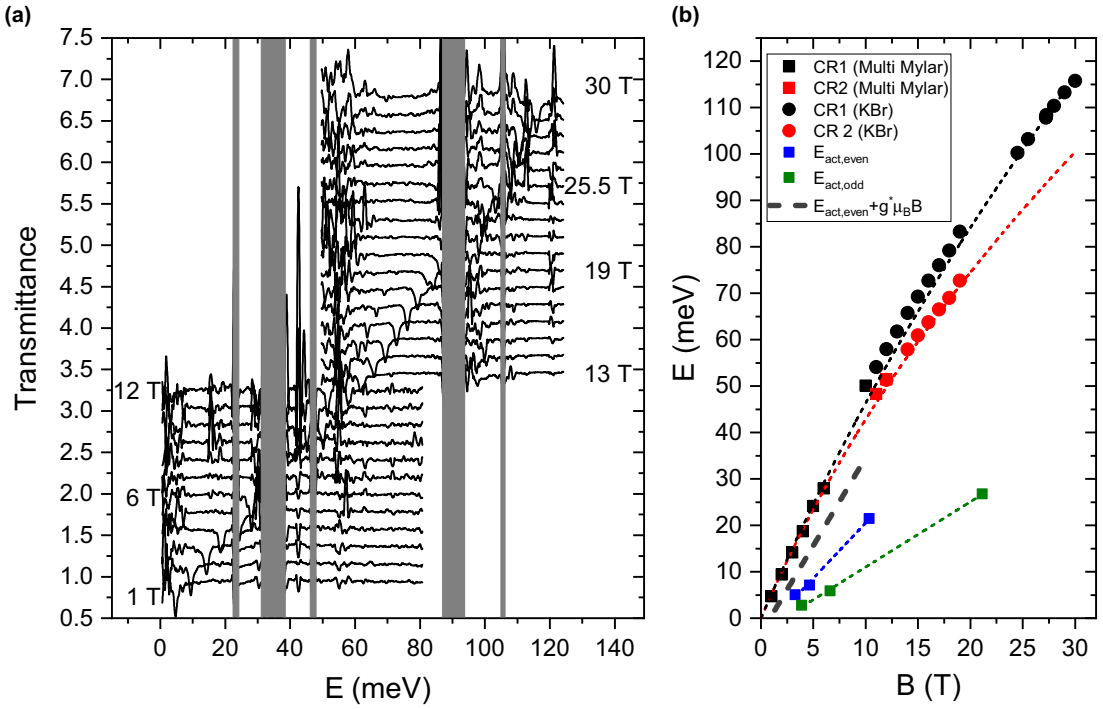

FIG. 11. (a) Transmittance as a function of wave number in an InSb QW for different magnetic fields. The traces have a constant offset of 0.2. The phonon absorption bands have been grayed out. In the field range between 11 and 18 T, there are two CR features corresponding to different LL transitions. (b) Cyclotron resonance energy as a function of magnetic field. Here, we used a multilayered Mylar beamsplitter for $E = 1 - 81$ meV and a KBr beamsplitter for $E = 50 - 124$ meV.

[1] K. v. Klitzing, G. Dorda, and M. Pepper, New method for high-accuracy determination of the fine-structure constant based on quantized Hall resistance, Phys. Rev. Lett. **45**, 494 (1980).

[2] D. C. Tsui and A. C. Gossard, Resistance standard using quantization of the Hall resistance of GaAs-$Al_xGa_{1-x}As$ heterostructures, Appl. Phys. Lett. **38**, 550 (1981).

[3] J. A. Alexander-Webber, A. M. R. Baker, P. D. Buckle, T. Ashley, and R. J. Nicholas, High-current breakdown of the quantum Hall effect and electron heating in InSb/AlInSb, Phys. Rev. B **86**, 045404 (2012).

[4] K. S. Novoselov, A. K. Geim, S. V. Morozov, D. Jiang, M. I. Katsnelson, I. V. Grigorieva, S. Dubonos, and A. A. Firsov, Two-dimensional gas of massless Dirac fermions in graphene, Nature (London) **438**, 197 (2005).

[5] D. A. Bandurin, A. V. Tyurnina, G. L. Yu, A. Mishchenko, V. Zólyomi, S. V. Morozov, R. K. Kumar, R. V. Gorbachev, Z. R. Kudrynskyi, S. Pezzini *et al.*, High electron mobility, quantum Hall effect and anomalous optical response in atomically thin InSe, Nat. Nanotechnol. **12**, 223 (2017).

[6] L. Li, F. Yang, G. J. Ye, Z. Zhang, Z. Zhu, W. Lou, X. Zhou, L. Li, K. Watanabe, T. Taniguchi *et al.*, Quantum Hall effect in black phosphorus two-dimensional electron system, Nat. Nanotechnol. **11**, 593 (2016).

[7] F. Tang, P. Wang, M. He, M. Isobe, G. Gu, Q. Li, L. Zhang, and J. H. Smet, Two-dimensional quantum Hall effect and zero energy state in few-layer $ZrTe_5$, Nano Lett. **21**, 5998 (2021).

[8] K. S. Novoselov, Z. Jiang, Y. Zhang, S. Morozov, H. L. Stormer, U. Zeitler, J. Maan, G. Boebinger, P. Kim, and A. K. Geim, Room-temperature quantum Hall effect in graphene, Science **315**, 1379 (2007).

[9] G. W. Small, B. W. Ricketts, P. C. Coogan, B. J. Pritchard, and M. M. R. Sovierzoski, A new determination of the quantized Hall resistance in terms of the NML calculable cross capacitor, Metrologia **34**, 241 (1997).

[10] A. Hartland, R. G. Jones, B. P. Kibble, and D. J. Legg, The relationship between the SI Ohm, the Ohm at NPL, and the quantized Hall resistance, IEEE Trans. Instrum. Meas. **IM-36**, 208 (1987).

[11] A.-M. Jeffery, R. Elmquist, L. H. Lee, J. Q. Shields, and R. F. Dziuba, NIST comparison of the quantized Hall resistance and the realization of the SI Ohm through the calculable capacitor, IEEE Trans. Instrum. Meas. **46**, 264 (1997).

[12] B. Jeckelmann and B. Jeanneret, The quantum Hall effect as an electrical resistance standard, Rep. Prog. Phys. **64**, 1603 (2001).

[13] T. J. B. M. Janssen, J. M. Williams, N. Fletcher, R. Goebel, A. Tzalenchuk, R. Yakimova, S. Lara-Avila, S. Kubatkin, and V. Fal'Ko, Precision comparison of the quantum Hall effect in graphene and gallium arsenide, Metrologia **49**, 294 (2012).

[14] R. Stradling, Magnetotransport and magnetooptics of $InAs_{1-x}Sb_x$ and heterojunctions combinations formed between InAs and GaSb, AlSb or $InAs_{1-x}Sb_x$, Acta Phys. Pol. A **92**, 851 (1997).

[15] I. Vurgaftman, J. Á. Meyer, and L. R. Ram-Mohan, Band parameters for III–V compound semiconductors and their alloys, J. Appl. Phys. **89**, 5815 (2001).

[16] Z. Lei, E. Cheah, K. Rubi, M. E. Bal, C. Adam, R. Schott, U. Zeitler, W. Wegscheider, T. Ihn, and K. Ensslin, High-quality two-dimensional electron gas in undoped InSb quantum wells, Phys. Rev. Res. **4**, 013039 (2022).

[17] Z. Lei, C. A. Lehner, K. Rubi, E. Cheah, M. Karalic, C. Mittag, L. Alt, J. Scharnetzky, P. Märki, U. Zeitler, W. Wegscheider, T. Ihn, and K. Ensslin, Electronic *g* factor and magnetotransport in InSb quantum wells, Phys. Rev. Res. **2**, 033213 (2020).

[18] J. C. Chokomakoua, N. Goel, S. J. Chung, M. B. Santos, J. L. Hicks, M. B. Johnson, and S. Q. Murphy, Ising quantum Hall ferromagnetism in InSb-based two-dimensional electronic systems, Phys. Rev. B **69**, 235315 (2004).

[19] S. Metti, C. Thomas, D. Xiao, and M. J. Manfra, Spin-orbit coupling and electron scattering in high-quality $InSb_{1-x}As_x$ quantum wells, Phys. Rev. B **106**, 165304 (2022).

[20] Y. Jiang, M. Ermolaev, S. Moon, G. Kipshidze, G. Belenky, S. Svensson, M. Ozerov, D. Smirnov, Z. Jiang, and S. Suchalkin, *g*-factor engineering with InAsSb alloys toward zero band gap limit, Phys. Rev. B **108**, L121201 (2023).

[21] S. Svensson, W. Beck, W. Sarney, D. Donetsky, S. Suchalkin, and G. Belenky, Temperature dependent Hall effect in InAsSb with a 0.11 eV 77 K-bandgap, Appl. Phys. Lett. **114** (2019).

[22] C. A. Lehner, On the limitations and prospects of MBE grown high-mobility InSb quantum wells, Doctoral thesis, ETH Zurich, Zurich (2019).

[23] C. A. Lehner, T. Tschirky, T. Ihn, W. Dietsche, J. Keller, S. Fält, and W. Wegscheider, Limiting scattering processes in high-mobility InSb quantum wells grown on GaSb buffer systems, Phys. Rev. Mater. **2**, 054601 (2018).

[24] Z. Lei, C. A. Lehner, E. Cheah, M. Karalic, C. Mittag, L. Alt, J. Scharnetzky, W. Wegscheider, T. Ihn, and K. Ensslin, Quantum transport in high-quality shallow InSb quantum wells, Appl. Phys. Lett. **115**, 012101 (2019).

[25] N. Miura, *Physics of Semiconductors in High Magnetic Fields*, Series on Semiconductor Science and Technology (Oxford University Press, Oxford, 2007).

[26] Y. B. Li, S. S. Dosanjh, I. T. Ferguson, A. G. Norman, A. G. de Oliveira, R. A. Stradling, and R. Zallen, Raman scattering in $InAs_{1-x}Sb_x$ alloys grown on GaAs by molecular beam epitaxy, Semicond. Sci. Technol. **7**, 567 (1992).

[27] T. Ihn, *Semiconductor Nanostructures: Quantum States and Electronic Transport* (Oxford University Press, Oxford, 2009).

[28] T. Khouri, M. Bendias, P. Leubner, C. Brüne, H. Buhmann, L. W. Molenkamp, U. Zeitler, N. E. Hussey, and S. Wiedmann, High-temperature quantum Hall effect in finite gapped HgTe quantum wells, Phys. Rev. B **93**, 125308 (2016).

[29] J. Zhu, H. L. Stormer, L. N. Pfeiffer, K. W. Baldwin, and K. W. West, Spin susceptibility of an ultra-low-density two-dimensional electron system, Phys. Rev. Lett. **90**, 056805 (2003).

[30] T. Englert, D. C. Tsui, A. C. Gossard, and C. Uihlein, *g*-factor enhancement in the 2d electron gas in GaAs/AlGaAs heterojunctions, Surf. Sci. **113**, 295 (1982).

[31] R. J. Nicholas, R. J. Haug, K. v. Klitzing, and G. Weimann, Exchange enhancement of the spin splitting in a GaAs-$Ga_xAl_{1-x}As$ heterojunction, Phys. Rev. B **37**, 1294 (1988).

[32] E. V. Kurganova, H. J. van Elferen, A. McCollam, L. A. Ponomarenko, K. S. Novoselov, A. Veligura, B. J. van Wees, J. C. Maan, and U. Zeitler, Spin splitting in graphene studied by means of tilted magnetic-field experiments, Phys. Rev. B **84**, 121407(R) (2011).

[33] T. Ando and Y. Uemura, Exchange enhancement of the spin splitting in a GaAs-$Ga_xAl_{1-x}As$ heterojunction, J. Phys. Soc. Jpn. **37**, 1044 (1974).

[34] T. Ando, A. B. Fowler, and F. Stern, Electronic properties of two-dimensional systems, Rev. Mod. Phys. **54**, 437 (1982).